Crustal deformation across the Southern Patagonian Icefield observed by GNSS

Article *in* Earth and Planetary Science Letters · October 2016

DOI: 10.1016/j.epsl.2016.07.042

12 authors, including:

Andreas Richter
Technische Universität Dresden
41 PUBLICATIONS **454** CITATIONS
SEE PROFILE

Erik R. Ivins
California Institute of Technology
163 PUBLICATIONS **5,090** CITATIONS
SEE PROFILE

Heiner Lange
Technische Universität Dresden
6 PUBLICATIONS **161** CITATIONS
SEE PROFILE

Luciano Pedro Oscar Mendoza
Universidad Nacional de La Plata
17 PUBLICATIONS **101** CITATIONS
SEE PROFILE

Earth and Planetary Science Letters 452 (2016) 206–215

Contents lists available at ScienceDirect

Earth and Planetary Science Letters

www.elsevier.com/locate/epsl

Crustal deformation across the Southern Patagonian Icefield observed by GNSS

A. Richter [a,b,c,*], E. Ivins [d], H. Lange [a], L. Mendoza [b,c], L. Schröder [a], J.L. Hormaechea [b,c,e], G. Casassa [f,g], E. Marderwald [b,c], M. Fritsche [a,h], R. Perdomo [b], M. Horwath [a], R. Dietrich [a]

[a] Technische Universität Dresden, Institut für Planetare Geodäsie, Dresden, Germany
[b] Universidad Nacional de La Plata, Facultad de Ciencias Astronómicas y Geofísicas, La Plata, Argentina
[c] CONICET, Argentina
[d] Jet Propulsion Laboratory, California Institute of Technology, Pasadena, USA
[e] Estación Astronómica Río Grande, Río Grande, Argentina
[f] Geoestudios, Santiago, Chile
[g] Universidad de Magallanes, Punta Arenas, Chile
[h] GFZ German Research Centre for Geosciences, Potsdam, Germany

ARTICLE INFO

Article history:
Received 16 March 2016
Received in revised form 19 July 2016
Accepted 23 July 2016
Available online xxxx
Editor: A. Yin

Keywords:
crustal deformation
glacial-isostatic adjustment
GNSS
Patagonia

ABSTRACT

Geodetic GNSS observations at 43 sites well distributed over the Southern Patagonian Icefield region yield site velocities with a mean accuracy of 1 mm/a and 6 mm/a for the horizontal and vertical components, respectively. These velocities are analyzed to reveal the magnitudes and patterns of vertical and horizontal present-day crustal deformation as well as their primary driving processes. The observed vertical velocities confirm a rapid uplift, with rates peaking at 41 mm/a, causally related to glacial-isostatic adjustment (GIA). They yield now an unambiguous preference between two competing GIA models. Remaining discrepancies between the preferred model and our observations point toward an effective upper mantle viscosity even lower than $1.6 \cdot 10^{18}$ Pa s and effects of lateral rheological heterogeneities. An analysis of the horizontal strain and strain-rate fields reveals some complex superposition, with compression dominating in the west and extension in the east. This deformation field suggests significant contributions from three processes: GIA, a western interseismic tectonic deformation field related to plate subduction, and an extensional strain-rate field related to active Patagonian slab window tectonics.

1. Introduction

The Southern Patagonian Icefield (SPI) has been identified as a locus of exceptionally rapid crustal uplift (Dietrich et al., 2010; Lange et al., 2014). Models show that observed vertical deformation in this region can be explained by glacial-isostatic adjustment (GIA) (Ivins and James, 1999, 2004; Klemann et al., 2007). Vertical site velocities observed in Patagonia exceed those reported for other regions affected by glacier retreat such as Alaska (Larsen et al., 2005), Greenland (Khan et al., 2007; Dietrich et al., 2005) and West Antarctica (Groh et al., 2012).

The large-amplitude GIA response in Patagonia results from the coincidence of a large, rapidly changing temperate ice mass and a unique tectonic setting. The Patagonian icefields, representing the largest extra-polar ice mass in the southern hemisphere, have experienced substantial fluctuations in glacier extent and mass throughout the Pleistocene (e.g. Strelin et al., 2011, 1999; Mercer, 1976) and Holocene (e.g. Strelin et al., 2014; Aniya, 2013; Masiokas et al., 2009) until present (e.g. Floricioiu et al., 2012; Willis et al., 2012; Glasser et al., 2011; Casassa et al., 2002). GIA models suggest, however, that the uplift observed today in Patagonia is caused by ice-mass changes since the Little Ice Age (LIA) with its maximum extent between AD 1630 and 1870 (Ivins and James, 2004; Lange et al., 2014). The uplift predicted from the elastic crustal response to ongoing ice loss shows a more localized pattern than the complete gravitational visco-elastic rebound, but may reach about half the total uplift rate close to fast-retreating glaciers like Upsala (Lange et al., 2014, Fig. 1c).

The short-lived memory of the solid earth for load changes in southern Patagonia, compared to other regions affected by GIA, is due to the peculiar regional rheology characterized by a thin lithosphere and very low viscosities in the asthenosphere and upper

* Corresponding author at: Technische Universität Dresden, Institut für Planetare Geodäsie, Dresden, Germany.
E-mail address: andreas.richter@tu-dresden.de (A. Richter).

http://dx.doi.org/10.1016/j.epsl.2016.07.042
0012-821X/

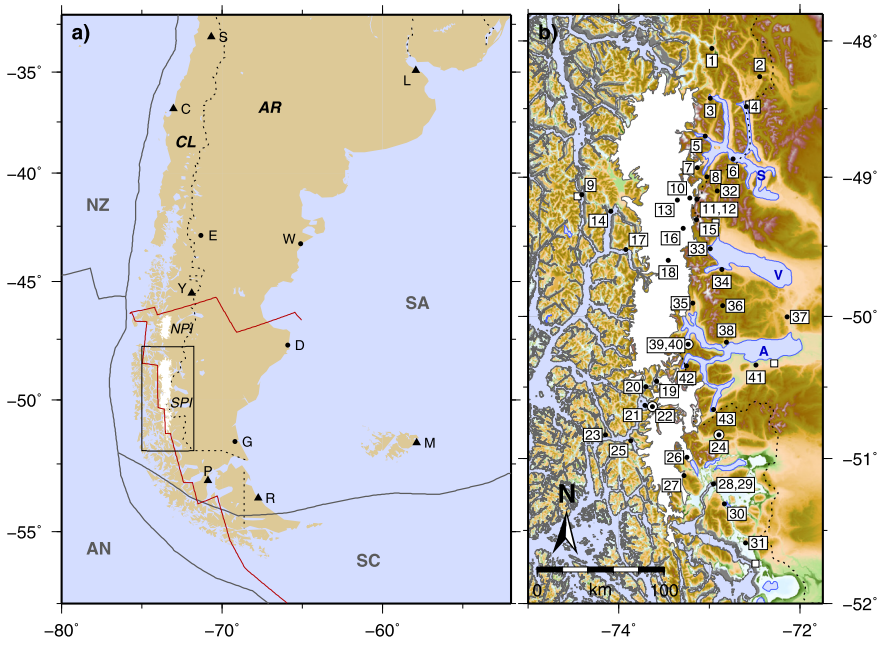

Fig. 1. Maps of the region under investigation. **a)** Location of the Northern (NPI) and Southern Patagonian Icefields (SPI) in southernmost South America. Triangles depict the IGS stations, dots RAMSAC stations included in the GNSS data processing. Grey lines show the boundaries of the tectonic plates Nazca (NZ), South America (SA), Antarctica (AN) and Scotia (SC) according to Bird (2003). Red lines delimit the Patagonian slab window according to Breitsprecher and Thorkelson (2009). Dotted line: national border between Chile (CL) and Argentina (AR). Box: area shown in the maps in Figs. 1b, 3 and 4. **b)** Topographic map of the SPI region. Black dots show the location of GNSS sites, numbers according to Table 1, numbers of sites 1–31 correspond to those in Lange et al. (2014). Dots with white circles: continuously logging GNSS sites. Lagos Argentino (A), Viedma (V) and San Martín/O'Higgins (S) are labeled as topographic reference. White boxes: towns, topography: SRTM digital elevation model (Rodriguez et al., 2005).

mantle (Lange et al., 2014). These rheological conditions, in turn, are imposed by the geologically young thermomechanics of the region. At the Chile Triple Junction, some 200 km NNW from the SPI, material of the relatively hot Chile Ridge is subducted beneath the South American plate (Fig. 1a). The subduction of this active spreading-ridge system between Nazca and Antarctic plates is accompanied by the opening of the Patagonian slab window. The existence and extent of this slab window has been established by geochemical analysis of Patagonian lavas and basalts (Gorring and Kay, 2001; Boutonnet et al., 2010), seismic imaging (Russo et al., 2010a; Gallego et al., 2010), shear wave splitting measurements (Murdie and Russo, 1999; Russo et al., 2010b) and plate kinematic modeling (Breitsprecher and Thorkelson, 2009). The slab window environment beneath the southernmost South American continent is characterized by upwelling of hot mantle material and enhanced mantle flow through the window with a strong ridge-parallel component (Russo et al., 2010b).

From structural-geological point of view, most of our sites pertain to the Southern Patagonian Andes fold-thrust belt. Most authors agree that fold deformation and activity of minor faults in our study area are of late-Miocene age or older (e.g. Giacosa et al., 2012; Fosdick et al., 2011; Ghiglione et al., 2009; Kraemer, 1998). Coutand et al. (1999) suspect that basement faults along the cordillera in the Lago Viedma area "appear to be active in strike-slip reverse mode". Currently, evidence for active faulting in the SPI region is difficult to find. International seismological catalogues (ISC, 2015; USGS, 2015; Villaseñor et al., 1997; Sabbione et al., 2007) report also only a small number and low magnitude of seismic events for this area. There are active volcanoes along the crest of the Southern Patagonian Andes. However, the deformation associated with volcanic activity is usually restricted to the vicinity of the volcano edifice, and none of our sites are located close enough to be affected by volcanic deformation. We assume, therefore, that our observed site velocities essentially represent the long-wavelength deformation field.

Both plate collision and slab window opening are expected in addition to GIA to produce large-scale surface deformations affecting the SPI region. Tectonic deformations are reflected primarily in the horizontal components (e.g., Elliott et al., 2010). However, previous works on crustal deformation in southern Patagonia focused on the vertical component (Dietrich et al., 2010; Lange et al., 2014). Global compilations of the horizontal deformation field, in turn, expose Patagonia as a region lacking geodetic observations (Kreemer et al., 2014).

This paper presents results of GNSS observations in a regional network of 43 sites. Compared to previous work, the network extension and geometry are improved and allow, for the first time, a detailed analysis of the horizontal velocity components. The observed vertical and horizontal site velocities are interpreted with regard to the magnitude, patterns and driving processes of present-day crustal deformation across the SPI.

2. Observations

The first geodetic GNSS observations in the area of the SPI were carried out as early as 1996 (Lange et al., 2014). Until 2001, seven sites were observed, mainly on top of the hard-to-reach icefield on Chilean territory. In 2003, a network of eight sites was set up in the area of Lago O'Higgins (Chile; "S" in Fig. 1b) in the northern part of the SPI for a systematic observation of GIA (Dietrich et al., 2010). This was complemented by a network of eleven sites set up in 2009 across the southern tip of the icefield (Lange et al., 2014). Since 2010 the setup and observation of new GNSS sites has been extended to Argentine territory, connecting the isolated networks to the north and south of the icefield. At present, 12 sites have been observed repeatedly on the Argentine side. The locations of the GNSS sites are shown in Fig. 1b.

All our markers are fixed in bedrock. The sites set up since 2003 provide for direct mounting of the GNSS antenna onto the marker. Five of the early sites were occupied using a tribrach while three

Table 1
GNSS sites in the SPI region. For each site, the number according to Fig. 1b, the coordinates, the years of the first and last observation, the number of campaign occupations, the accumulated total amount of daily observation files and the north (N), east (E) and up (U) velocity components with their estimated uncertainties σ are given. Numbers of sites 1–31 correspond to those in Lange et al. (2014). "C" in column 8 denotes a continuously logging GNSS site.

Site	Lat. S		Lon. W		First observation	Last observation	Campaigns	Data [d]	V_N [mm/a]	$\pm\sigma_{V_N}$ [mm/a]	V_E [mm/a]	$\pm\sigma_{V_E}$ [mm/a]	V_U [mm/a]	$\pm\sigma_{V_U}$ [mm/a]
	[°]	[′]	[°]	[′]										
1	48	3.32	72	58.39	2003	2010	4	31	13.0	0.54	6.4	0.58	22.5	3.87
2	48	15.93	72	26.63	2003	2010	4	38	12.0	0.54	7.5	0.58	18.7	3.86
3	48	25.50	72	59.41	2003	2010	3	24	13.1	0.54	7.4	0.58	26.8	3.87
4	48	29.08	72	35.64	2003	2010	6	121	12.4	0.54	6.0	0.58	21.3	3.86
5	48	42.12	73	2.78	2003	2010	3	24	12.9	0.54	8.3	0.58	29.7	3.87
6	48	52.05	72	44.42	2003	2010	3	21	12.1	0.54	9.3	0.58	24.9	3.87
7	48	55.86	73	8.06	2006	2010	2	15	12.1	0.93	7.0	1.01	30.5	5.23
8	48	59.83	73	1.70	2003	2010	5	73	14.5	0.54	7.4	0.58	33.4	3.87
9	49	7.57	74	24.54	2008	2011	2	6	7.8	1.20	9.3	1.29	3.1	10.78
10	49	9.05	73	13.03	1998	2010	3	4	10.8	0.31	5.7	0.34	41.0	4.27
11	49	9.51	73	8.33	2003	2010	5	41	11.1	0.54	7.3	0.58	34.6	3.88
12	49	9.61	73	8.39	1998	2010	3	10	11.9	0.31	8.7	0.33	39.0	4.26
13	49	9.98	73	21.16	2007	2010	2	8	13.2	1.23	3.0	1.32	33.1	6.25
14	49	14.75	74	5.23	1996	2011	3	16	9.9	0.25	6.9	0.27	17.7	3.86
15	49	18.43	73	8.55	2001	2010	2	7	10.5	0.42	9.1	0.45	33.2	5.05
16	49	22.29	73	17.38	2001	2010	2	5	9.6	0.42	4.5	0.45	38.3	5.06
17	49	31.26	73	55.27	2006	2011	2	12	13.4	1.14	1.6	1.19	20.4	8.30
18	49	35.95	73	27.25	1996	2010	3	9	9.7	0.27	2.8	0.29	28.2	3.94
19	50	27.56	73	34.98	2009	2011	2	8	8.4	1.75	6.9	1.88	15.9	8.05
20	50	29.83	73	42.07	2008	2011	4	16	9.4	0.97	4.6	1.05	7.0	5.37
21	50	37.75	73	42.56	2009	2011	3	14	12.5	1.74	7.0	1.88	6.0	8.03
22	50	38.19	73	37.66	2009	2011	C	737	10.5	1.74	9.2	1.88	10.7	8.04
23	50	50.09	74	8.75	2009	2011	3	17	10.0	1.74	8.9	1.88	9.2	8.03
24	50	50.17	72	53.63	2009	2012	C	864	11.9	1.55	8.8	1.67	7.9	7.38
25	50	52.65	73	51.91	2009	2011	3	17	9.2	1.74	8.6	1.88	7.1	8.03
26	50	59.52	73	14.87	2009	2014	3	29	10.7	0.83	10.7	0.90	16.9	4.88
27	51	7.14	73	16.78	2009	2011	2	22	10.0	1.75	9.5	1.89	16.8	8.06
28	51	10.64	72	57.19	1999	2009	2	6	11.2	0.37	10.5	0.40	5.2	4.72
29	51	10.68	72	57.11	2009	2014	4	34	11.0	0.83	10.0	0.90	6.5	4.89
30	51	19.00	72	50.06	2009	2011	3	29	11.0	1.77	6.7	1.91	6.5	8.14
31	51	35.02	72	35.97	2009	2011	3	23	12.2	1.77	7.5	1.91	2.3	8.14
32	49	5.92	72	54.73	2012	2014	3	24	12.0	1.88	9.0	2.02	18.1	8.49
33	49	30.98	72	59.51	2011	2014	3	20	11.5	1.22	8.8	1.32	26.6	6.24
34	49	39.97	72	51.89	2011	2014	4	29	10.5	1.23	11.1	1.32	21.2	6.25
35	49	54.37	73	10.91	2010	2014	5	35	7.8	0.93	10.5	1.00	26.8	5.21
36	49	55.52	72	51.21	2011	2014	4	27	9.4	1.21	12.0	1.30	19.7	6.19
37	50	0.29	72	8.52	2011	2014	4	29	11.7	1.22	7.7	1.32	5.3	6.24
38	50	11.07	72	48.63	2011	2014	2	15	9.1	1.19	10.1	1.29	14.5	6.13
39	50	11.83	73	14.07	2011	2014	4	13	9.6	1.20	8.3	1.29	22.5	6.14
40	50	11.88	73	14.05	2012	2014	C	494	8.8	2.71	6.9	2.92	18.2	11.39
41	50	20.81	72	29.11	2011	2014	4	41	10.4	1.19	8.4	1.29	9.9	6.13
42	50	21.11	73	15.14	2010	2014	5	37	9.1	0.93	8.6	1.00	15.8	5.20
43	50	39.44	72	57.18	2011	2014	3	21	11.3	1.23	7.8	1.32	7.7	6.24

further early points were observed using a tripod (Lange et al., 2014). During all occupations geodetic GPS receivers and antennas were employed to log dual-frequency code and phase observations. Starting in 2009, part of the equipment also supported GLONASS in addition to GPS. In order to minimize systematic effects, the same antenna was used during all occupations of the individual sites. This was not possible for nine of the earliest sites (Lange et al., 2014). Occupations were mainly carried out in campaign style and generally involved several complete 24 h sessions per campaign. A few exceptions to this rule were imposed by logistic challenges of the early observations interior to the icefield at high elevation. Usually all occupations of a site were carried out at the same time of the year in order to reduce the impact of seasonal effects on the determination of site velocities.

In this work, we make use of GNSS observation data of 43 regional sites. The 31 sites on Chilean territory are the same used by Lange et al. (2014), with new observations added for two sites (26, 29). These data are complemented for the first time by observations of 12 sites in Argentina. Three of our sites (22, 24, 40) are continuously logging stations (Fig. 1b). The remaining sites accumulate on average 24 daily observation sessions distributed over slightly more than three campaign occupations each. The average time span between the first and last observation on these regional sites is 5 yrs. Table 1 summarizes the observational data used in this study. In addition to our regional network, continuous GNSS data of eight permanent stations of the global network of the International GNSS Service (IGS) and four stations of the Argentine RAMSAC network (Red Argentina de Monitoreo Satelital Continuo, by IGN, 2015) are introduced in the data processing to link our observations to the IGS08 terrestrial reference frame (Rebischung et al., 2012) (Fig. 1a).

3. Analysis

3.1. GNSS data processing

The entire set of GNSS data was processed using the Bernese GNSS Software 5.1 (Dach et al., 2007). Products derived from a joint reprocessing of global GPS, GLONASS and SLR data (Fritsche et al., 2014), including IGS station coordinates, satellite orbits and earth orientation parameters, are introduced and provide state-of-the-art consistency and stability. Absolute phase-center corrections are applied for both satellite and receiver antennas. The Vienna mapping function (Kouba, 2008) and 2-hourly zenith delay estimates are used to correct for the tropospheric delay. Higher-order ionospheric delays are accounted for following the approach de-

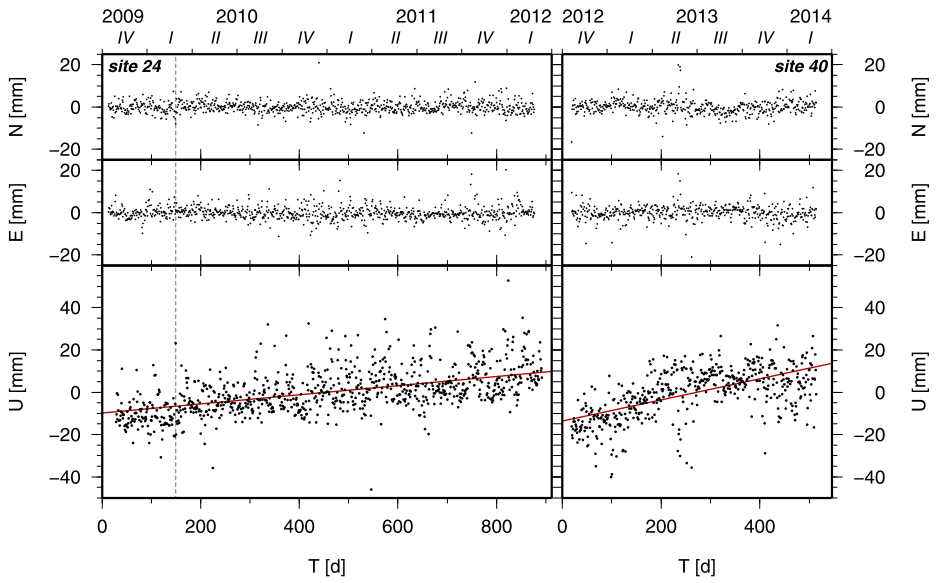

Fig. 2. Position time series determined at the continuous GNSS sites 24 (left) and 40 (right). Residual daily positions, corrected for tidal and non-tidal atmospheric and ocean loading, after subtraction of the derived linear position model are shown for the North (top) and East (center) components. Bottom: observed daily vertical positions. Red line: derived linear position model (i.e. vertical velocity). Time is shown in quarters (top) and days (bottom), vertical dashed line: date of the Mw 8.8 Maule earthquake. (Note that site 40 is regarded the least accurate in our regional network.)

scribed by Fritsche et al. (2005). Corrections for solid-earth tide, ocean-tidal loading (Savcenko and Bosch, 2012) and tidal atmospheric loading are applied. In addition, we applied the 6-hourly GRACE AOD1B de-aliasing product (GFZ, 2015) to correct for non-tidal atmospheric and ocean loading. The products of the global reprocessing by Fritsche et al. (2014) are available only until 2013. Therefore, operational products provided by the IGS for 2014 are used to include also the data acquired during the last campaign (early 2014). In order to assess the impact of this change in the set of products on the derived site velocities, the observations between 2003 and 2013 are additionally processed using the operational IGS products. The comparison with the velocities obtained for this interval applying our reprocessed products yields velocity differences below 2 mm/a and 1 mm/a for the vertical and horizontal components, respectively.

3.2. Estimation of confidence intervals

Daily normal equations are formed based on double-difference phase observations. These daily normal equations are stacked in a combined solution yielding a mean position and velocity for each site and coordinate component. In addition, the daily normal equations are solved also individually yielding time series of daily positions for each site and coordinate component. Fig. 2 shows the time series of daily positions for the two regional continuous stations 24 and 40. The position time series of further sites are shown in the supplementary material. The residual position time series (i.e. after removing the linear position change implied by the obtained velocities) of our three regional continuous stations (22, 24, 40) are used to derive individual uncertainty estimates for each site and velocity component. Based on these residual time series the standard deviation of a single daily position solution in the three coordinate components is determined accounting for temporal correlations (Williams, 2008). We obtain daily positioning accuracies of 2.6 mm, 2.8 mm and 9.0 mm for the north, east and up components, respectively. For the sites and occupations, where the antenna was not directly mounted onto the marker, a 10 mm antenna eccentricity uncertainty is added in all three coordinate components (Table 1). The positioning uncertainties are then propagated for each site individually to its velocity estimates according to the time span between first and last observation day. The disregard of the actual amount of observation days within this time span makes this a conservative accuracy estimate. For the vertical velocity component, a 2 mm/a reference frame uncertainty is added (Bevis and Brown, 2014). An alternative approach to estimate trends and their uncertainties in GNSS time series by determining and incorporating their actual autocorrelation (Nilsson and Elgered, 2008) confirms our velocity uncertainty estimates as conservative. The resultant site velocities, along with their site-specific uncertainty estimates, are included in Table 1. On average the uncertainties obtained for the N, E and vertical components amount to 1.1 mm/a, 1.1 mm/a and 6.0 mm/a, respectively.

Throughout the time covered by our GNSS observations, the Maule Mw 8.8 earthquake (February 27, 2010) has been the event with the greatest potential to produce jumps in the position time series that would affect our velocity estimates (ISC, 2015; USGS, 2015; Sabbione et al., 2007). However, no significant change in the behavior of the time series of our continuously operated sites is observed at that date (Fig. 2 left; suppl. material). In addition, careful inspection of our time series does not reveal any transient deformation signal. Moreover, the application of the MIDAS velocity estimator (Blewitt et al., 2016), designed to be resistant to coordinate jumps, confirms our velocities. We conclude that in the region under investigation and throughout the observation time span neither co-seismic or post-seismic deformation reach sufficient amplitude to affect our velocity estimates and that the observed (horizontal) site velocities represent interseismic crustal deformation rates.

3.3. Strain analysis

In order to quantitatively characterize the horizontal surface deformation in the region under investigation, the approach of Mendoza et al. (2015) is applied to derive a locally uniform strain rate field from the observed horizontal site velocities. The three components of the strain rate tensor (ε_{ee}; ε_{nn}; ε_{en}), together with a rigid rotation rate, are estimated for each point of a regular grid of 5 km spacing. The inversion involves a least-squares adjustment, in which the observed velocities are reweighted by a factor of $A\exp(-d/\sigma)$. Here, A weights the contribution of each GNSS

Table 2
Characteristics of the GIA models A and B from Lange et al. (2014).

Model	Lithosph. thickness [km]	Viscosity [Pa s]	Ice-load history: piecewise linear mass loss rates [Gt/a]				
			1630–1869	1870–1943	1944–1975	1976–1994	1995–2013
A	36.5	$1.6 \cdot 10^{18}$	0.0	−11.2	−4.5	−8.6	−10.7
B	36.5	$8 \cdot 10^{18}$	−0.009	−6.8	−4.7	−10.5	−25.9

site according to the area of its corresponding cell in a Voronoi tessellation of the site locations, d is the distance between the site and the grid point being evaluated and σ is a smoothing factor chosen to be 50 km. For each grid element the second invariant of the strain rate is calculated as $\sqrt{(\varepsilon_{ee}^2 + \varepsilon_{nn}^2 + 2\varepsilon_{en}^2)}$ (Kreemer et al., 2003). For an identical grid the standard deviation of this second invariant is derived by formal propagation of the uncertainties of the observed horizontal velocity components. Finally, a grid of the signal-to-noise ratio of the second invariant of strain-rate is derived by point-wise dividing the second invariant value by its standard deviation (Kreemer et al., 2014).

3.4. GIA modeling

We employ regional models of the glacial-isostatic adjustment to explain our observed vertical velocities. These models predict the GIA-induced present-day vertical deformation rate as the gravitational visco-elastic response of the solid earth to past and present changes of the ice mass in the Patagonian icefields. The forward modeling requires the introduction of a load model, which describes the ice-load history in space and time, and an earth model, which quantifies the response of the solid earth to an applied force. We compare our observational results to the two regional models of GIA-induced vertical deformation rate presented in Lange et al. (2014). These models result from a series of progressive refinement of the regional ice-load history and adjustment of the effective earth model parameters (Ivins and James, 1999; Ivins and James, 2004; Dietrich et al., 2010; Ivins et al., 2011; Lange et al., 2014). The earth model consists of a Maxwellian visco-elastic half-space beneath an elastic lithosphere. The parameters of the model that have greatest sensitivity to the data are the lithospheric thickness and the viscosity of a homogeneous mantle. The ice-load model comprises the evolution of ice mass in the SPI and NPI back in time to the Pleistocene Llanquihue glaciations. Previous works have shown, however, that the observable present-day deformation in Patagonia is almost completely due to the ice-mass changes since the Little Ice Age.

The two models, referred to as model A and B, represent the end members of the search in the earth model parameter space (lithospheric thickness, mantle viscosity) for an optimum fit of the modeled deformation rates to observed uplift rates. Both models differ in the underlying post-LIA ice-load histories as well as in the mantle viscosity yielding the optimum model fit. The total ice mass lost since the LIA maximum is identical for both models, but the distribution of the mass loss rates in time is different for both cases. Model A assumes moderate present-day mass loss, but wasting rates immediately following the LIA maximum exceeding slightly the present ones. This model implies a very low viscosity of $1.6 \cdot 10^{18}$ Pa s. Model B, in turn, is characterized by vast present-day mass loss rates more than twice those of model A and relatively small historic ice-mass losses. It allows for a somewhat more prevalent mantle viscosity of $8 \cdot 10^{18}$ Pa s. Despite their significant differences in ice-mass loss timing and mantle viscosity, both models produce an almost equal fit with the set of observed uplift rates used in Lange et al. (2014). Both competing models coincide consistently in the best-fit lithospheric thickness of 36.5 ± 5.3 km. Models A and B are summarized in Table 2.

4. Results

4.1. Vertical velocities

The vertical velocities observed at our GNSS sites, together with their estimated uncertainties, are included in Table 1 and displayed in Fig. 3a. All the observed vertical velocities are positive, indicating uplift with respect to the global reference frame. They range from 2.3 mm/a at our southernmost site 31 to 41.0 mm/a at site 10. The site-specific uncertainties of the vertical velocities range from 3.9 to 11.4 mm/a. The consistency found in general between neighboring sites suggests that the observed variation in the vertical velocities is dominated by a common, long-wavelength pattern. It consists of a dome-like uplift distribution, with its center at the eastern margin of the SPI between Lagos Viedma and San Martín/O'Higgins, and from where the uplift rate decreases in all directions.

4.2. Mean horizontal velocity vector

The horizontal velocity components of our regional sites relative to the IGS08 terrestrial reference frame are dominated by a common movement. The mean velocity vector of the regional sites amounts to 13.4 mm/a directed 35.6° NNE (Fig. 4a, black vector). This common horizontal movement primarily reflects the motion of the South American tectonic plate with respect to the IGS08 reference frame. Among the permanent IGS/RAMSAC sites included in this study we chose six (E, W, G, M, A, R) to derive the rotation vector of the rigid South American plate from their horizontal velocity components. We obtain an Euler pole at 37°19′S, 108°18′W with a rotation rate of 0.243°/Ma and residuals of the introduced horizontal velocities below 2 mm/a. The green vector in Fig. 4a shows the horizontal motion implied by this rigid plate rotation for the average coordinates of our regional sites. This rigid plate motion vector (green) differs from the mean horizontal velocity vector (black) by a difference vector (mean minus plate rotation) of 5.2 mm/a towards 90.3°E. This difference reflects the fact, that our regional network does not belong to the rigid portion of the South American plate, but rather is affected by a common, large scale deformation.

4.3. Residual horizontal velocities

The residual horizontal site velocities after subtraction of the mean velocity vector (black) from the observed horizontal velocity components are shown in Fig. 4a in red. The maximum residual velocity is 6.7 mm/a (site 17; i.e. half the mean horizontal velocity with respect to the terrestrial reference frame), and the average of the 43 residual velocities is 2.3 mm/a (i.e. almost half of the deviation of the mean velocity vector from the rigid plate motion). The residual velocity vectors are dominated by a general pattern, pointing radially away from a center located close to the eastern margin of the SPI about halfway between Lagos Viedma and San Martín/O'Higgins. A distinct exception from this pattern is revealed by our westernmost sites 9 and 14, and in a less extent also

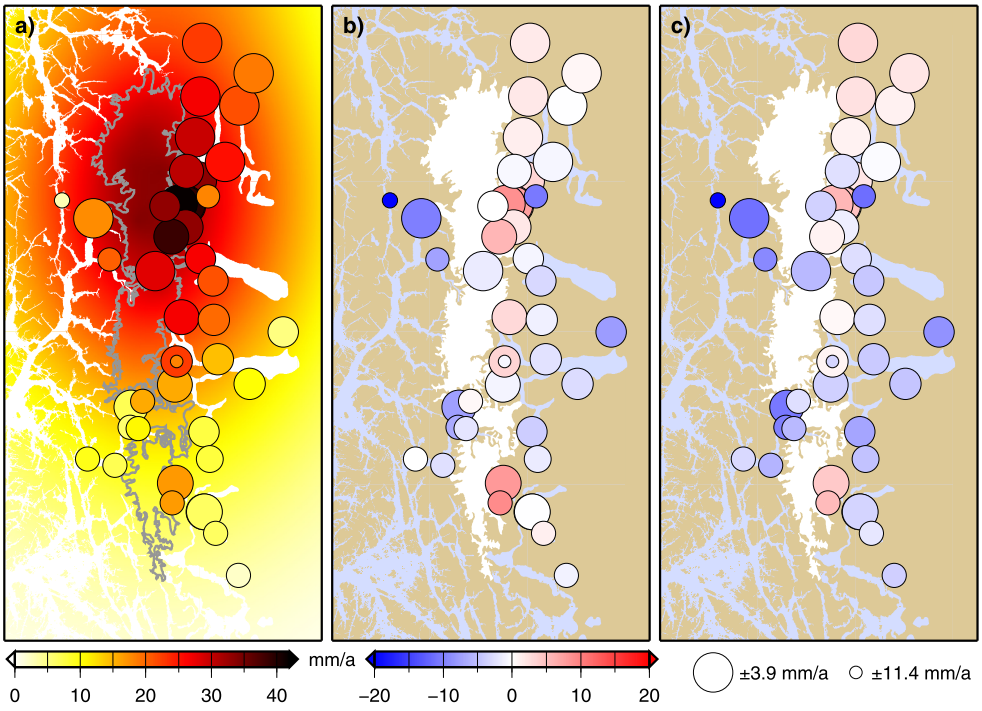

Fig. 3. Vertical site velocities. **a)** The vertical velocities observed at our GNSS sites are shown as colored dots. Size of the dots indicates the estimated accuracy of the vertical velocity (see scale at the bottom, right). Background shows in the same color scale the vertical crustal deformation predicted by GIA model A in Lange et al. (2014). Grey line: SPI. **b)** Residual vertical velocities after subtraction of the GIA model A prediction from the observed vertical velocities. White area: SPI. **c)** Same as b) after subtraction of the GIA model B (Lange et al., 2014) prediction from the observed vertical velocities.

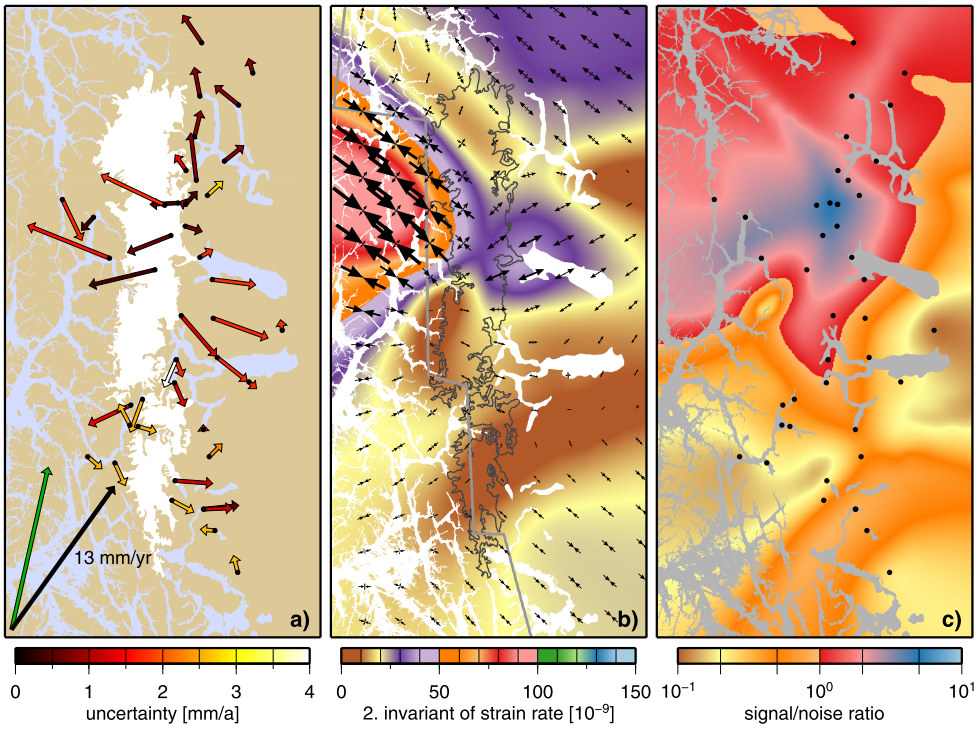

Fig. 4. Horizontal site velocities and deformation. **a)** Residual horizontal site velocities after subtraction of the mean velocity from the observed velocities. Color of the vectors indicates their estimated uncertainty. The subtracted mean velocity vector is shown in black at the bottom, left. Green vector: velocity implied by the derived rigid plate rotation at the mean network position. White area: SPI. **b)** Strain map. Color shows the second invariant of the strain rate, strain crosses indicate the type and (by size) magnitude of surface deformation. Dark grey line: SPI, light grey line: Antarctic slab edge according to Breitsprecher and Thorkelson (2009). **c)** Signal-to-noise ratio of the second invariant of strain rate (Fig. 4b). Black dots: GNSS sites.

23 and 25, featuring a dominant SSE orientation. However, these residual velocity vectors depend in their magnitude and orientation on the choice of their reference (here: the mean velocity of our regional network) and are therefore difficult to interpret. The general pattern of residual horizontal velocity vectors emanating away from the center of uplift is consistent with what is gener-

ally predicted for late-Holocene rebound following century-long ice losses (see Fig. 9b in Ivins et al., 2002).

4.4. Strain-rate map

The strain map in Fig. 4b depicts the horizontal surface deformation independently from any datum definition. The background color shows the second invariant of the strain-rate tensor and the vector crosses indicate the magnitude and orientation of the maximum extension (minimum compression) and maximum compression (minimum extension). The map in Fig. 4c shows the signal-to-noise ratio as obtained by point-wise dividing the second invariant of the strain rate by its estimated uncertainty (Kreemer et al., 2014). Over most of the area shown, the second invariant of the strain-rate remains below $50 \cdot 10^{-9}$ a^{-1}, i.e. 5 mm per year over 100 km. Within the area encompassed by our GNSS sites, the uncertainty does not reach $25 \cdot 10^{-9}$ a^{-1}, but increases, as expected, towards the periphery of our network. The deformation pattern is characterized by a transition from a roughly E–W directed compression in the west to a roughly E–W directed extension in the east. This transition in the deformation regime is accompanied by a local minimum of the second invariant of the strain-rate and coincides approximately with the main axis of the SPI. Over the eastern part of our network the deformation regime changes orientation from north to south. In the north there is NW–SE directed extension (around Lago San Martín/O'Higgins), via SW–NE directed extension (around Lago Viedma) to NW–SE directed compression (south of Lago Argentino).

A striking compression signal, responsible also for the maximum of the strain second invariant of up to $100 \cdot 10^{-9}$ a^{-1}, is revealed in the Pacific fjords at the latitudes between Lagos Viedma and San Martín/O'Higgins, at the western margin of our region under investigation. The westernmost portion of the mapped deformation anomaly is not constrained by observation sites. Nevertheless, the SE part of the anomaly is supported by the horizontal motions of three GNSS sites, and the exclusion of any of these sites from the strain analysis does not remove this anomaly. It can, therefore, not be explained as an artifact due to observation errors or local effects of an individual site, but should be recognized as actual signal (as indicated by the signal-to-noise ratio in Fig. 4c).

5. Discussion

5.1. Vertical velocities

Fig. 3a shows the observed vertical velocities together with the vertical deformation predicted by the GIA model A in Lange et al. (2014). The general agreement between model and observations, especially regarding the concentrical, dome-shaped uplift pattern, demonstrates that the visco-elastic response to regional ice-mass changes since the LIA is the primary process reflected in the vertical velocities. This model results from a fit, via the adjustment of the earth model parameters, to a subset of our GNSS data. The general consistency in the magnitude of the predicted and observed uplift rates is therefore not surprising. Nevertheless, the pattern of uplift is governed by the applied ice-load history and the physics of the solid earth response (both independent from the GNSS observations).

Fig. 3b depicts the residual vertical velocities after subtracting model A from the observational results. It shows an approximate balance between positive and negative residuals. The maximum and minimum residuals amount to +9.16 mm/a and −20.33 mm/a, respectively, and the mean weighted misfit (Larsen et al., 2005) is 0.05. Fig. 3c shows in analogy the residual vertical velocities after subtraction of model B. In this case the residuals are primarily negative, suggesting that model B overestimates the uplift rates over most of the area. The maximum and minimum residuals of +5.71 mm/a and −19.98 mm/a, respectively, are slightly smaller compared to model A. However, the mean weighted misfit of 0.41 exceeds clearly that for model A. The more limited set of observations used by Lange et al. (2014) provided less discriminatory information for supporting one model over another. From a glaciological and tectonic point of view, model A was regarded as less plausible. However, our extended and updated set of uplift observations yields now a clear preference for this model. It thus favors an extremely low effective viscosity, a more moderate present-day ice mass loss and a rapid deglaciation during the decades following the LIA maximum, when more total ice at lower elevations was highly unstable in the face of a changing climate. Should, however, new data emerge that provide for a refinement of the ice-load history model this would lead to a further improvement of the estimate of mantle viscosity.

Nevertheless, the distribution of the residuals in Fig. 3b reveals remaining systematic discrepancies of this model: positive residual velocities are concentrated along the eastern edge of the SPI, while negative residuals are found to the east and west beyond the icefield. It suggests: 1) a westward shift of the modeled locus of maximum uplift (center of the icefield) compared to the observations (eastern margin of the icefield); 2) a slight underestimation of the maximum uplift; and 3) a smoother decay of the uplift rate at the flanks of the icefield than observed. The more localized uplift, as suggested by the observed steeper slopes of the radial decay, as well as the larger maximum uplift rate point toward an even lower effective viscosity and/or lithospheric thickness than implied by model A. The observed offset of the uplift maximum towards the east from the load center (i.e. SPI central axis), as well as a steeper uplift decay across the western flank than to the east, indicate an asymmetry in the visco-elastic response predicted by Klemann et al. (2007) as a consequence of lateral variations in the lithosphere/mantle rheology. In fact, accounting for a subducting slab, low-viscosity zones in the fore-arc mantle wedge and a ductile layer near the base of the continental crust (10^{18} Pa s both), and an asthenosphere (10^{19} Pa s), their model reproduces important features which would improve the fit of model A to our observations, in particular, a more localized uplift and asymmetrically steeper uplift gradients to the west than to the east of the load (Fig. 5 in Klemann et al., 2007). Additional, or alternative, causes for the observed eccentricity of the uplift maximum with respect to the main axis of the SPI could be an underestimation of the ice-mass loss the at eastern flank of the SPI by the ice-load model used by Lange et al. (2014) and the rather sparse spatial sampling by our GNSS sites at high elevation within the icefield.

5.2. Horizontal displacements and deformation

Previous quantitative information on the present-day horizontal surface deformation in southern Patagonia was limited to global strain models. The global strain-rate model by Kreemer et al. (2014) indicates for this region a roughly constant second invariant of the strain rate at the $64 \cdot 10^{-9}$ a^{-1} level and contraction as the prevailing deformation regime. These results, however, are based on very few observations in southern Patagonia. Our regional GNSS network provides for the first time a reliable, detailed picture of the surface deformation in this geodynamically complex environment. In our strain-rate map (Fig. 4b) the second invariant is below $50 \cdot 10^{-9}$ a^{-1} over most of the area. Although contraction is indeed responsible for the maximum deformation, it is confined to a small area, while extension dominates the major part of the region. Past global models of this scalar representation of the deformation field in southern Patagonia were unable to resolve the spatial variations that are revealed by our new data.

In fact, our strain-rate map depicts an intricate structure of diverse deformation regimes which results from the superposition of the effects of different processes.

The relatively intense compression in the west is consistent with the expected interseismic tectonic deformation. The NW–SE direction of the principal compression axis agrees approximately with the relative convergent motion of the Antarctic with respect to the South American plate. In addition, the difference between the network's mean horizontal velocity vector (black vector in Fig. 4a) and the vector of rigid plate rotation (green vector) suggests that the bulk of our GNSS sites is affected by the plate collision resulting in a common eastward movement of the entire network with respect to the rigid South American plate. However, at a distance of 200 to 300 km from the trench a smooth and relatively homogeneous strain-rate field would be expected, with NW–SE dominated compression rates roughly constant parallel to the trench and decreasing towards E. The narrow localization of the intense compression in our strain map, in part, owes to the limited distribution of our GNSS sites. Both the northern and southern extent of our network does not sample the strain field close to the trench, and the cluster to the SW (sites 19–23, 25) is less sensitive for NW–SE deformations as indicated by the signal-to-noise ratio (Fig. 4c). Nevertheless, this effect cannot explain why extension is observed over most of the area that is so well sampled by our network. Consequently, additional processes must contribute to the observed deformation.

The glacial-isostatic adjustment, with its efficiency clearly evidenced in the vertical deformation, is expected to produce a radial pattern with minimum horizontal strain at the uplift maximum and extension directed away from the uplift center (e.g., Ivins et al., 2002; Ivins and James, 2004, suppl. mat.). Indeed, our strain map reveals a minimum of the second invariant in the area of the SPI. However, this strain minimum is situated some 150 km to the SSW from the uplift maximum. To the east and north of this strain-rate minimum the observed extension direction is in concert with the expected GIA-induced deformation pattern. The compression observed to the west of the strain minimum, however, cannot be explained by GIA. We suspect that both the compression prevailing to the west of the strain minimum, and the shift of the strain minimum with respect to the uplift maximum, result from the superposition of the GIA-induced deformation with the far-field tectonic deformation of the converging plates.

We might additionally conclude that the complex ties transferred to the crust/lithosphere from transient slab-window mantle dynamics are either longer wavelength than our network coverage, or that these have migrated to the NE, as in several tectonic models. However, the combination of GIA and simple plate convergence processes fail to explain the widespread extension throughout the eastern part of our network with directions essentially unaligned with the uplift maximum or strain minimum. We interpret this stretching as the surface effect of enhanced flow and upwelling of mantle material through the Patagonian slab window (Gorring and Kay, 2001; Breitsprecher and Thorkelson, 2009; Boutonnet et al., 2010; Russo et al., 2010a, 2010b). The transition from observed compression to extension coincides indeed with the location of the Antarctic slab edge according to Breitsprecher and Thorkelson (2009) (Fig. 4b). The NW–SE directed extension observed north of Lago San Martín/O'Higgins might be caused by an enhanced mantle flow focused along the central axis of the slab window (following roughly the projection of the ridge beyond the Chile Triple Junction). The existence of this SE directed mantle flow through the slab window is supported by fast polarization directions determined by Murdie and Russo (1999). The change in the extension orientation to SW–NE observed further to the south, in turn, may indicate that off the axis of focused flow the spreading component associated with the opening of the ridge and window becomes prominent. This assumption is confirmed by explicit regional 3D model simulation of mantle circulation (Lin, 2014). These simulations establish the viability of a small-scale toroidal circulation and a flow that has a transition between trench-normal and trench-parallel flow direction. These predicted patterns are supported by inferences of fan-shaped patterns of seismic anisotropy (Russo et al., 2010a, 2010b). The flow velocities presented by Lin (2014) for the uppermost layers (her Figs. 5a, 5d and 11), however, are roughly one order of magnitude too large (cm/a) to be consistent with our residual site velocities and strain rates observed at the surface (mm/a), and this may be due to weak coupling either at the top of the asthenosphere or near the base of the lower crust.

6. Conclusions

Our GNSS network extents for the first time into Argentina and completes now a circumferential coverage around the SPI. The observed vertical velocities confirm a rapid uplift with a maximum rate slightly exceeding 4 cm/a and GIA as the primary cause (Lange et al., 2014; Dietrich et al., 2010). But our updated and extended data set yields now an unambiguous preference for one of the two competing GIA models presented by Lange et al. (2014). And the improved network geometry allows now also the interpretation of the horizontal velocities.

The observed velocities reveal the contribution of three major processes: GIA, plate tectonics and the opening of the Patagonian slab window. They document a dual interaction between the peculiar tectonic situation and the visco-elastic response to ice-load changes: First, a mechanical superposition of the characteristic patterns of each of the three processes, which results in the complex composite of horizontal deformation revealed by our strain analysis. And second, the lateral differentiation of the glacial-isostatic response imposed by the three-dimensional rheological structure and mantle flow as revealed by the observed localized, asymmetric uplift pattern. The mantle circulation, in turn, is affected by the load-induced movement of mantle material. Future improvement in modeling and understanding the present-day crustal deformation in southern Patagonia calls for careful integration of the three processes that we have identified here from observations, within a three-dimensional, time-dependent framework of rheological structure and mantle circulation.

Acknowledgements

The German part of the project was funded by the German Research Foundation DFG (grants RI 2340/1-1, DI 473/40-1). E. Ivins was funded at the Jet Propulsion Laboratory, California Institute of Technology, by the Cryosphere Program, the Earth Surface and Interior Focus Area and as part of both the GRACE Science and NASA Sea-level Change Teams. We thank Gerardo Connon, Luis Barbero, Anja Wendt, Andrés Rivera, Rodrigo Traub, Marcelo Arévalo and Hans Silva for their valuable help in the field. We thank the administrations of Parque Nacional Los Glaciares, Parque Nacional Torres del Paine, CONAF and DIFROL for support, advice and permission of our field activities. Logistic support was provided by Prefectura Naval Lago Argentino, Estancia Cristina, Patagonia Expeditions El Chaltén, Hostería Grey and the crews of motor boat Soberanía and ferry boat Integración. We thank two anonymous reviewers and the editor Dr. An Yin for their valuable suggestions, which helped to improve this paper.

Appendix A. Supplementary material

Supplementary material related to this article can be found online at http://dx.doi.org/10.1016/j.epsl.2016.07.042.

References

Aniya, M., 2013. Holocene glaciations of Hielo Patagonico (Patagonia Icefield), South America. A brief review. Geochem. J. 47, 97–105.

Bevis, M., Brow, A., 2014. Trajectory models and reference frames for crustal motion geodesy. J. Geod. 88 (3), 283–311. http://dx.doi.org/10.1007/s00190-013-0685-5.

Bird, P., 2003. An updated digital model of plate boundaries. Geochem. Geophys. Geosyst. 4. http://dx.doi.org/10.1029/2001GC000252.

Blewitt, G., Kreemer, C., Hammond, W.C., Gazeaux, J., 2016. MIDAS robust trend estimator for accurate GPS station velocities without step detection. J. Geophys. Res., Solid Earth 121, 2054–2068. http://dx.doi.org/10.1002/2015JB012552.

Boutonnet, E., Arnaud, N., Guivel, C., Lagabrielle, Y., Scalabrino, B., Espinoza, F., 2010. Subduction of the South Chile active spreading ridge: a 17 Ma to 3 Ma magmatic record in central Patagonia (western edge of Meseta del Lago Buenos Aires, Argentina). J. Volcanol. Geotherm. Res. 189, 319–339. http://dx.doi.org/10.1016/j.jvolgeores.2009.11.022.

Breitsprecher, K., Thorkelson, D.J., 2009. Neogene kinematic evolution of the Nazca–Antarctic–Phoenix-slab windows beneath Patagonia and the Antarctic Peninsula. Tectonophysics 464, 10–20. http://dx.doi.org/10.1016/j.tecto.2008.02.013.

Casassa, G., Rivera, A., Aniya, M., Naruse, R., 2002. Current knowledge of the Southern Patagonia Icefield. In: Casassa, G., Sepúlveda, F., Sinclair, R. (Eds.), The Patagonian Icefields: A Unique Natural Laboratory for Environmental and Climate Change Studies, Series of the Centro de Estudios Científicos. Kluwer Academic/Plenum Publishers, New York, pp. 67–83.

Coutand, I., Diraison, M., Cobbold, P., Gapais, D., Rosello, E., Miller, M., 1999. Structure and kinematics of a foothills transect, Lago Viedma, southern Andes (49°30′). J. South Am. Earth Sci. 12, 1–15.

Dach, R., Hugentobler, U., Fridez, P., Meindl, M. (Eds.), 2007. Bernese GPS Software Version 5.0. Astronomical Institute Univ. of Bern, Switzerland.

Dietrich, R., Rülke, A., Scheinert, M., 2005. Present-day vertical crustal deformations in West Greenland from repeated GPS observations. Geophys. J. Int. 163, 865–874. http://dx.doi.org/10.1111/j.1365-246X.2005.02766.x.

Dietrich, R., Ivins, E., Casassa, G., Lange, H., Wendt, J., Fritsche, M., 2010. Rapid crustal uplift in Patagonia due to enhanced ice loss. Earth Planet. Sci. Lett. 289, 22–29. http://dx.doi.org/10.1016/j.epsl.2009.10.021.

Elliott, J.L., Larsen, C.F., Freymueller, J.T., Motyka, R.J., 2010. Tectonic block motion and glacial isostatic adjustment in southeast Alaska and adjacent Canada constrained by GPS measurements. J. Geophys. Res. 115, B09407. http://dx.doi.org/10.1029/2009JB007139.

Floricioiu, D., Abdel, J.W., Rott, H., 2012. Surface elevation changes and velocities on the Southern Patagonia Icefield derived from TerraSAR-X and TanDEM-X. Paper presented at ESA CLiC EO Cyosphere ESRIN, Frascati.

Fosdick, J.C., Romans, B.W., Fildani, A., Bernhardt, A., Calderon, M., Graham, S.A., 2011. Kinematic evolution of the Patagonian retroarc fold-and-thrust belt and Magallanes foreland basin, Chile and Argentina, 51°30′S. Geol. Soc. Am. Bull. 123, 1679–1698.

Fritsche, M., Dietrich, R., Knöfel, C., Rülke, A., Vey, S., Rothacher, M., Steigenberger, P., 2005. Impact of higher-order ionospheric terms on GPS estimates. Geophys. Res. Lett. 32, L23311. http://dx.doi.org/10.1029/2005GL024342.

Fritsche, M., Sosnica, K., Rodriguez-Solano, C.J., Steigenberger, P., Wang, K., Dietrich, R., Dach, R., Hugentobler, U., Rothacher, M., 2014. Homogeneous reprocessing of GPS, GLONASS and SLR observations. J. Geod. 88 (7), 625–642. http://dx.doi.org/10.1007/s00190-014-0710-3.

Gallego, A., Russo, R.M., Comte, D., Mocanu, V.I., Murdie, R.E., Vandecar, J.C., 2010. Seismic noise tomography in the Chile ridge subduction region. Geophys. J. Int. 182, 1478–1492. http://dx.doi.org/10.1111/j.1365-246X.2010.04691.x.

Ghiglione, M., Suarez, F., Ambrosio, A., Da Poian, G., Cristallini, E., Pizzio, M., Reinoso, M., 2009. Structure and evolution of the Austral Basin fold-thrust belt, southern Patagonian Andes. Rev. Asoc. Geol. Argent. 65 (1), 215–236.

Giacos, R., Fracchia, D., Heredi, N., 2012. Structure of the Southern Patagonian Andes at 49°S, Argentina. Geol. Acta 10 (3), 265–282. http://dx.doi.org/10.1344/105.000001749.

Glasser, N., Harrison, S., Jansson, K., Anderson, K., Cowley, A., 2011. Global sea-level contribution from the Patagonian Icefields since the Little Ice Age maximum. Nat. Geosci. 4, 303–307. http://dx.doi.org/10.1038/ngeo1122.

Gorring, M.L., Kay, S.M., 2001. Mantle sources and processes of Neogene slab window magmas from southern Patagonia, Argentina. J. Petrol. 42, 1067–1094.

Groh, A., Ewert, H., Scheinert, M., Fritsche, M., Rülke, A., Richter, A., Rosenau, R., Dietrich, R., 2012. An investigation of glacial isostatic adjustment over the Amundsen Sea sector, West Antarctica. Glob. Planet. Change 98–99, 45–53. http://dx.doi.org/10.1016/j.gloplacha.2012.08.001.

Ivins, E., James, T., 1999. Simple models for late Holocene and present-day Patagonian glacier fluctuations and predictions of a geodetically detectable isostatic response. Geophys. J. Int. 138 (3), 601–624.

Ivins, E., James, T., 2004. Bedrock response to Llanquihue Holocene and present-day glaciation in southernmost South America. Geophys. Res. Lett. 31, L24613. http://dx.doi.org/10.1029/2004GL021500.

Ivins, E.R., Raymond, C.A., James, T.S., 2002. Late-Pleistocen, Holocene and present-day ice load evolution in the Antarctic Peninsula: models and predicted vertical crustal motion. In: Mitrovica, J.X., Vermeersen, B. (Eds.), Ice Sheets, Sea Level and the Dynamic Earth. In: Geodyn. Ser., vol. 29. AGU, Washington, DC, pp. 133–155.

Ivins, E., Watkins, M., Yuan, D.-N., Dietrich, R., Casassa, G., Rülke, A., 2011. On-land ice loss and glacial isostatic adjustment at the Drake Passage: 2003–2009. J. Geophys. Res. 116, B02403. http://dx.doi.org/10.1029/2010JB007607.

Khan, S., Wahr, J., Stearns, L., Hamilton, G., van Dam, T., Larson, K., Francis, O., 2007. Elastic uplift in southeast Greenland due to rapid ice mass loss. Geophys. Res. Lett. 34, L21701. http://dx.doi.org/10.1029/2007GL031468.

Klemann, V., Ivins, E., Martinec, Z., Wolf, D., 2007. Models of active glacial isostasy roofing warm subduction: case of the South Patagonian Ice field. J. Geophys. Res. 112, B09405. http://dx.doi.org/10.1029/2006JB004818.

Kouba, J., 2008. Implementation and testing of the gridded Vienna Mapping Function 1 (VMF1). J. Geod. 82, 193–205. http://dx.doi.org/10.1007/s00190-007-0170-0.

Kraemer, P.E., 1998. Structure of the Patagonian Andes: regional balanced cross section at 50°S, Argentina. Int. Geol. Rev. 40, 896–915.

Kreemer, C., Holt, W.E., Haines, A.J., 2003. An integrated global model of present-day plate motions and plate boundary deformation. Geophys. J. Int. 154, 8–34. http://dx.doi.org/10.1046/j.1365-246X.2003.01917.x.

Kreemer, C., Blewitt, G., Klein, E.C., 2014. A geodetic plate motion and Global Strain Rate Model. Geochem. Geophys. Geosyst. 15, 3849–3889. http://dx.doi.org/10.1002/2014GC005407.

Lange, H., Casassa, G., Ivins, E.R., Schröder, L., Fritsche, M., Richter, A., Groh, A., Dietrich, R., 2014. Observed crustal uplift near the Southern Patagonian Icefield constrains improved viscoelastic Earth models. Geophys. Res. Lett. 41. http://dx.doi.org/10.1002/2013GL058419.

Larsen, C.F., Motyka, R.J., Freymueller, J.T., Echelmeyer, K.A., Ivins, E.R., 2005. Rapid viscoelastic uplift in southeast Alaska caused by post-little Ice Age glacial retreat. Earth Planet. Sci. Lett. 237, 548–560. http://dx.doi.org/10.1016/j.epsl.2005.06.032.

Lin, S.-C., 2014. Three-dimensional mantle circulations and lateral slab deformation in the southern Chilean subduction zone. J. Geophys. Res., Solid Earth 119, 3879–3896. http://dx.doi.org/10.1002/2013JB010864.

Masiokas, M., Rivera, A., Espizua, L., Villalba, R., Delgado, S., Aravena, J., 2009. Glacier fluctuations in extratropical South America during the past 1000 years. Palaeogeogr. Palaeoclimatol. Palaeoecol. 281, 242–268. http://dx.doi.org/10.1016/j.palaeo.2009.08.006.

Mendoza, L., Richter, A., Fritsche, M., Hormaechea, J.L., Perdomo, R., Dietrich, R., 2015. Block modeling of crustal deformation in Tierra del Fuego from GNSS velocities. Tectonophysics 651, 58–65. http://dx.doi.org/10.1016/j.tecto.2015.03.013.

Mercer, J.H., 1976. Glacial history of southernmost South America. Quat. Res. 6, 125–166.

Murdie, R.E., Russo, R.M., 1999. Seismic anisotropy in the region of the Chile Margin Triple Junction. J. South Am. Earth Sci. 12, 261–270. http://dx.doi.org/10.1016/S0895-9811(99)00018-8.

Nilsson, T., Elgered, G., 2008. Long-term trends in the atmospheric water vapor content estimated from ground-based GPS data. J. Geophys. Res. 113, D19101. http://dx.doi.org/10.1029/2008JD010110.

Rebischung, P., Griffiths, J., Ray, J., Schmid, R., Collilieux, X., Garayt, B., 2012. IGS08: the IGS realization of ITRF2008. GPS Solut., vol. 16, pp. 483–494.

Rodriguez, E., Morris, C.S., Belz, J.E., Chapin, E.C., Martin, J.M., Daffer, W., Hensley, S., 2005. An assessment of the SRTM topographic products. Technical report, NASA, Jet Propulsion Laboratory D-31639.

Russo, R.M., Gallego, A., Comte, D., Mocanu, V.I., Murdie, R.E., VanDecar, J.C., 2010a. Source-side shear wave splitting and upper mantle flow in the Chile Ridge subduction Region. Geology 38, 707–710. http://dx.doi.org/10.1130/G30920.1.

Russo, R.M., VanDecar, J.C., Comte, D., Mocanu, V.I., Gallego, A., Murdie, R.E., 2010b. Subduction of the Chile Ridge: upper mantle structure and flow. GSA Today 20, 4–10. http://dx.doi.org/10.1130/GSATG61A.1.

Sabbione, N., Connon, G., Buffoni, C., Hormaechea, J.L., 2007. Tierra del Fuego reference standard earthquake catalogue. In: Proceedings of the Geosur 2007 International Geological Congress on the Southern Hemisphere. Santiago de Chile.

Savcenko, R., Bosch, W., 2012. EOT11a – empirical ocean tide model from multi-mission satellite altimetry. Technical Report DGFI 89. Deutsches Geodätisches Forschungsinstitut, Alfons-Goppel-Str. 11, D-80539 München, Germany.

Strelin, J.A., Re, G., Keller, R., Malagnino, E.C., 1999. New evidences concerning the Plio-Pleistocene landscape evolution of southern Santa Cruz region. J. South Am. Earth Sci. 12, 333–341.

Strelin, J.A., Denton, G.H., Vandergoes, M.J., Ninnemann, U.S., Putnam, A.E., 2011. Radiocarbon chronology of the late-glacial Puerto Bandera moraines, Southern Patagonian Icefield, Argentina. Quat. Sci. Rev. 30, 2551–2569.

Strelin, J.A., Kaplan, M.R., Vandergoes, M.J., Denton, G.H., Schaefer, J.M., 2014. Holocene glacier history of the Lago Argentino basin, Southern Patagonian Icefield. Quat. Sci. Rev. 101, 124–145. http://dx.doi.org/10.1016/j.quascirev.2014.06.026.

Villaseñor, A., Bergman, E.A., Boyd, T.M., Engdahl, E.R., Frazier, D.W., Harden, M.M., Orth, J.L., Parkes, R.L., Shedlock, K.M., 1997. Toward a comprehensive catalog of global historical seismicity. Eos Trans. AGU 78 (50), 581–588.

Williams, S.D.P., 2008. CATS: GPS coordinate time series analysis software. GPS Solut. 12 (2), 147–153. http://dx.doi.org/10.1007/s10291-007-0086-4.

Willis, M., Melkonian, A., Pritchard, M., Rivera, A., 2012. Ice loss from the South-

ern Patagonian Ice Field, South America, between 2000 and 2012. Geophys. Res. Lett. 39, L17501. http://dx.doi.org/10.1029/2012GL053136.

Internet references

GFZ, 2015. GRACE AOD1B. http://www.gfz-potsdam.de/en/aod1b.

IGN, 2015. Red Argentina de Monitoreo Satelital Continuo (RAMSAC). http://ign.gob.ar/category/tem%C3%A1tica/geodesia/ramsac.

ISC, 2015. International Seismological Centre. http://www.isc.ac.uk/iscbulletin/search/catalogue/.

USGS, 2015. The Preliminary Determination of Epicenters (PDE) Bulletin. http://earthquake.usgs.gov/data/pde.php.